
HETEROGENEOUS ANGULAR SPECTRUM METHOD FOR TRANS-SKULL IMAGING AND FOCUSING

Scott Schoen Jr

Woodruff School of Mechanical Engineering
Georgia Institute of Technology
Atlanta, GA USA
scottschoenjr@gatech.edu

Costas D. Arvanitis

Woodruff School of Mechanical Engineering and Coulter Department of Biomedical Engineering
Georgia Institute of Technology and Emory University
Atlanta, GA, USA
costas.arvanitis@gatech.edu

November 19, 2019

© 2020 IEEE. Personal use of this material is permitted. Permission from IEEE must be obtained for all other uses, in any current or future media, including reprinting/republishing this material for advertising or promotional purposes, creating new collective works, for resale or redistribution to servers or lists, or reuse of any copyrighted component of this work in other works. Article DOI: 10.1109/TMI.2019.2953872.

ABSTRACT

Ultrasound, alone or in concert with circulating microbubble contrast agents, has emerged as a promising modality for therapy and imaging of brain diseases. While this has become possible due to advancements in aberration correction methods, a range of applications, including adaptive focusing and tracking of the microbubble dynamics through the human skull, may benefit from even more computationally efficient methods to account for skull aberrations. Here, we derive a general method for the angular spectrum approach (ASA) in a heterogeneous medium, based on a numerical marching scheme to approximate the full implicit solution. We then demonstrate its functionality with simulations for (human) skull-related aberration correction and trans-skull passive acoustic mapping. Our simulations show that the general solution provides accurate trans-skull focusing as compared to the uncorrected case (error in focal point location of 1.0 ± 0.4 mm vs 2.2 ± 0.7 mm) for clinically relevant frequencies (0.25–1.5 MHz), apertures (50–100 mm), and targets, with peak focal pressures approximately $30 \pm 17\%$ of the free field case, with the effects of skull attenuation and amplitude shading included. In the case of source localization, our method leads to an average of 75 % error reduction (from 2.9 ± 1.8 mm to 0.7 ± 0.5 mm) and 40–60 % increase in peak intensity, evaluated over the range of frequencies (0.4–1.2 MHz), apertures (50–100 mm), and point source locations (40 mm by 50 mm grid) as compared to the homogeneous medium ASA. Overall, total computation times for both focusing and point source localization of the order milliseconds (166 ± 37 ms, compared with 44 ± 4 ms for the homogeneous ASA formulation) can be attained with this approach. Collectively our findings indicate that the proposed phase correction method based on the ASA could provide a computationally efficient and accurate method for trans-skull transmit focusing and imaging of point scatterers, potentially opening new possibilities for treatment and diagnosis of brain diseases.

1 Introduction

Ultrasound has emerged as a novel modality for the treatment and imaging of brain diseases and disorders [1, 2]. When enhanced by circulating microbubble contrast agents—lipid, albumin, or polymer-shelled gas pockets (1–10 μm) that scatter sound and vibrate in response to incident ultrasound—it can enable a range of new therapeutic interventions [3–8] and open new possibilities for imaging [9–11]. This has been facilitated by advancements in methods to account for skull aberrations.

In their simplest form, aberrations introduced by the skull may be corrected with knowledge of phase and amplitude at the transmitter due to a point source at the target, that can then be conjugated to achieve trans-skull focusing on transmit. Such phase and amplitude modulations may be determined experimentally via measurement of the field due to an induced cavitation source at the target location inside the skull [12–14], however cavitation events in the brain are not always desirable, and the relatively high cavitation threshold requires additional corrections or high power arrays [15]. Use of corrections based on analysis of time domain signals measured from contrast agent microbubble emissions has been demonstrated [16], though the location of these cavitation events cannot be controlled precisely. Alternatively, a point source can be placed within the skull to enable effective trans-skull therapy [17–20]; however this technique requires invasive placement at the target, which is not possible in realistic scenarios. For these reasons, several simulation techniques have been proposed for aberration correction, including finite difference time domain (FDTD) [21, 22] and k-space propagation models [23–25]. In these methods, the simulation of the acoustic propagation due to a point source inside the brain is used to estimate the required phases for aberration correction. While these methods can be very precise, as they may account for a broad range of physical effects including, e.g., mode conversion, viscosity and nonlinearity, there exists a fundamental trade-off between their accuracy and required computational complexity [26].

Currently an effective trade-off is obtained by the use of a stepwise, locally homogeneous angular spectrum approach (ASA), which employs either coordinate rotations to account for refraction [23] or accounts for spatial heterogeneity in the space domain before spectral propagation [27]. While these ASA implementations currently provide a reasonable compromise between computational complexity and aberration correction, they do not solve intrinsically the full wave propagation problem [26–29].

Inherently related to the problem of errors in trans-skull FUS targeting due to skull aberrations is that of source localization. This problem has emerged as a priority in microbubble enhanced US therapy and imaging: when exposed to ultrasound, microbubbles scatter diverging pressure waves that, due to their size (several orders of magnitude smaller than the wavelength), act as point sources. The information carried by these waves can enable the spatiotemporal characterization of the microbubble dynamics. During therapeutic interventions, this information is used to ensure that the desired type of oscillation (i.e., stable or inertial) is taking place at the intended location (i.e. treatment monitoring) [30].

Several approaches based on passive acoustic mapping (PAM) techniques have been proposed for monitoring the microbubble dynamics. While direct implementations do not account for aberrations [30–33], recent work has successfully incorporated human skull aberration corrections into both frequency-domain [34] and time-domain [11, 26, 35–38] PAM implementations. These methods require either measurement (invasive) [14, 17], simulations to calculate delays for each point in the image, or a representative point to be used for a local region [26, 39], which incurs a computational expense that scales with the field of view. These methods are thus either infeasible or time consuming (up to several minutes) unless GPUs are used to speed up the computations [26]. This problem can potentially be overcome with the ASA method [30], however current implementations do not account for aberrations.

The spectral selectivity inherent to frequency domain methods such as the ASA [30, 33] is important for characterizing the type of oscillation (e.g. harmonics vs broadband). However current implementations assume a homogeneous medium. In addition to spectral selectivity, reconstructions on the order of milliseconds are important for closed-loop control of the microbubble dynamics [40] and improved temporal resolution during microbubble imaging. [10, 35] While time domain methods [31, 32, 38] can readily incorporate corrections and extract for certain frequency content via filtering, they generally incur high computational loads, unless GPU units are used to speed up the computations [38]. Hence, fast and frequency selective reconstructions to visualize the cerebrovascular microbubble dynamics through the skull may have important implications for image guided therapy and imaging [8].

Herein we derive the general solution for the heterogeneous ASA. First, we present the derivation of a fast phase correction method for arbitrarily distributed, weakly heterogeneous medium. Then, through simulated acoustic propagation, we show the numerical implementation of the algorithm for focal aberration correction and frequency selective passive mapping of point sources through a human skull. Next, we evaluate the focal aberration error, focal pressure, and spot size, as well as the point source localization error and intensity, compared with the corresponding uncorrected cases. Finally, we evaluate the computational cost of the different algorithm permutations.

2 Theory

2.1 Angular Spectrum Approach

The angular spectrum P of a monochromatic¹ pressure field \tilde{p} with angular frequency ω is given by its 2D spatial Fourier transform

$$\begin{aligned} P(k_x, k_y, z) &= \mathcal{F}_k[\tilde{p}(x, y, z)] \\ &\equiv \iint_{-\infty}^{\infty} \tilde{p}(x, y, z) e^{-i(k_x x + k_y y)} dx dy. \end{aligned} \quad (1)$$

Applying the spatial transform to the homogeneous Helmholtz equation $(\nabla^2 + k^2)\tilde{p} = 0$ yields an ordinary differential equation for the angular spectrum

$$\frac{d^2 P}{dz^2} + k_z^2 P = 0, \quad (2)$$

where $k_z^2 = (\omega/c_0)^2 - k_x^2 - k_y^2$, and c_0 is the (constant) small signal sound speed. If P_0 is known at some reference plane $z = 0$, and if there are no backward-travelling waves, then Eq. (2) has the solution

$$P = P_0 e^{ik_z z}. \quad (3)$$

The acoustic field in any plane may then be reconstructed with Eq. (3) and evaluation of the inverse transform.

2.2 Extension to Heterogeneous Media

In the case of relatively weak heterogeneity—i.e. the sound speed $c(\mathbf{r})$ changes slowly compared with the wavelength—the governing equation is

$$\frac{d^2 P}{dz^2} + k_z^2 P = \Lambda * P. \quad (4)$$

Here, $\Lambda = \mathcal{F}_k [k_0^2(1 - \mu)]$, $k_0 = \omega/c_0$, $\mu = c_0^2/c^2$, c_0 is a reference (average) sound speed, and $*$ denotes a 2D convolution over the wavenumber components k_x and k_y . From Eq. (2), the heterogeneity appears as a source term in the governing equation. In the general case, the implicit solution of Eq. (4) may be obtained with a Green's function technique

$$P = P_0 e^{ik_z z} + \frac{e^{ik_z z}}{2ik_z} \int_0^z e^{-ik_z z'} (\Lambda * P) dz'. \quad (5)$$

A numerical approximation of Eq. (5) may be made to compute P at arbitrary z via

$$P^{n+1} \approx P^n e^{ik_z \Delta z} + \frac{e^{ik_z \Delta z}}{2ik_z} (P^n * \Lambda) \times \Delta z, \quad (6)$$

where $P^n = P(k_x, k_y, n\Delta z)$. See Appendix A for derivations of Eqs. (4) to (6). Previously, Gu and Jing persented a general forward propagation scheme for field simulations that includes nonlinearity and attenuation [41]. In the absence of these effects, Eq. (12) of that reference becomes (with the notation of this paper)

$$M = \mathcal{F}_k \left\{ \left[k_0^2 \left(1 - \frac{c_0^2}{c^2} \right) \right] \times \tilde{p} \right\} = \Lambda * P. \quad (7)$$

Substitution of this value of M into their Eq. (11) recovers Eq. (5) obtained here, indicating the consistency of the results.

3 Methods

3.1 Simulations

Acoustic propagation (either to evaluate the transmit focusing achieved with the computed time delays or to acquire the RF data to be used with the corrected beamforming) was simulated in k-Wave [42]. As the incident angles were largely

¹A time convention of $p = \tilde{p} e^{-i\omega t}$ is used, so that the forward temporal transform uses a kernel of $e^{+i\omega t}$, and that of the forward spatial transform is then $e^{-i(k_x x + k_y y)}$. The factors of $1/2\pi$ are applied on the inverse transforms.

below the critical angle for skull bone ($\sim 26^\circ$ [43]), elastic effects were not included in the simulation. The skull and tissue densities were computed from CT data of a human skull, and the spatially-dependent sound speed and absorption coefficient α were computed from the Hounsfield scale conversion as described previously [21, 37]. Absorption was included via a power law model $\alpha(\mathbf{r}) = \alpha_0(\mathbf{r}) \cdot f^\beta$ [44]. A power law exponent of $\beta = 1.2$ was defined for the entire medium [45], as k-Wave's implementation does not allow spatial variation of this parameter. Spatial grid spacing $200 \mu\text{m}$ and time step 40 ns were used for all simulations (CFL number $c\Delta t/\Delta x = 0.44$), and 2000 time steps ($80 \mu\text{s}$) were simulated. The reference sound speed was taken to be the average value over the entire grid. All reconstruction and aberration correction scripts were written in MATLAB and run on a standard desktop computer (Intel Core i7, four cores at 2.8 GHz and 16 GB memory) without parallel or graphical processing techniques. The general computational flows for focal aberration correction and source localization are shown in Fig. 1 and Fig. 2, respectively. While the correction can function in 3 dimensions [see, e.g., Fig. 2(c)], due to the large number of simulations required, simulations were performed in 2D (60 mm by 80 mm, with 10 point perfectly matched layer) for computational efficiency. Thus in the reconstructions $k_y = 0$.

3.2 Numerical Implementation

3.2.1 Transmit Focusing

To determine the improvement in focal aberration correction through human skull with the proposed general solution (heterogeneous ASA), the focusing delays were computed with and without phase corrections for clinically relevant frequencies (0.25–1.5 MHz) [2, 5, 46, 47]. To achieve focusing at a desired depth d , $P(k_x, d)$ was computed for a delta function at the desired focus, i.e., for $P_0 = \mathcal{F}_k[\delta(x - x_0, 0)]$. To avoid very steep changes on the spatial computation grid for the corrected case, this delta function was approximated as a cosine-windowed Gaussian distribution with full width at half maximum of 1.5 mm. Since the field is monochromatic, the excess phase represents the total time delay τ for an array element as a function of its position along the transducer face

$$\tau(x) = \frac{\arg \tilde{p}(x, d)}{\omega}. \quad (8)$$

Phase unwrapping was used to preserve the full phase of P at the transducer location. For reference, the results of focusing using the delays calculated with Eq. (8) were compared with the results obtained without accounting for medium heterogeneity (i.e., geometrical focusing). In this case, the delays were computed with $c_0 = 1500 \text{ m/s}$ directly from the target point via

$$\tau(x) = \frac{\sqrt{(x - x_0)^2 + d^2}}{c_0}. \quad (9)$$

The excitation time series for each element was a 40-cycle sine pulse with 100 kPa amplitude at the desired frequency, modulated with a Tukey window with $R = 0.1$, and shifted by the amount given by Eq. (8) [or Eq. (9) in the uncorrected

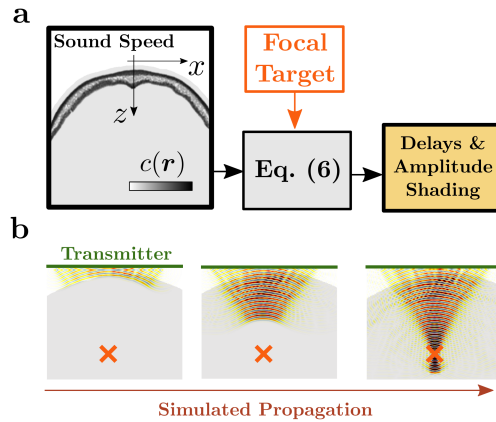


Figure 1: Flow of computations for focal aberration correction. (a) The known sound speed field $c(\mathbf{r})$ is used, together with the target focal spot, to compute the element amplitudes and time delays. (b) The delays and amplitudes are then used to simulate propagation and the location of peak intensity is compared with the target point.

case]. The relative amplitude for each element was scaled according to the normalized amplitude of $\tilde{p}(x, d)$ (or unity in the geometric case); the maximum amplitude of the corrected case was set to be 20 % larger than the uncorrected case due to the tapering of the outer elements. The field was then simulated with each element of the array transmitting with the calculated phase delay and amplitude.

3.2.2 Passive Acoustic Mapping

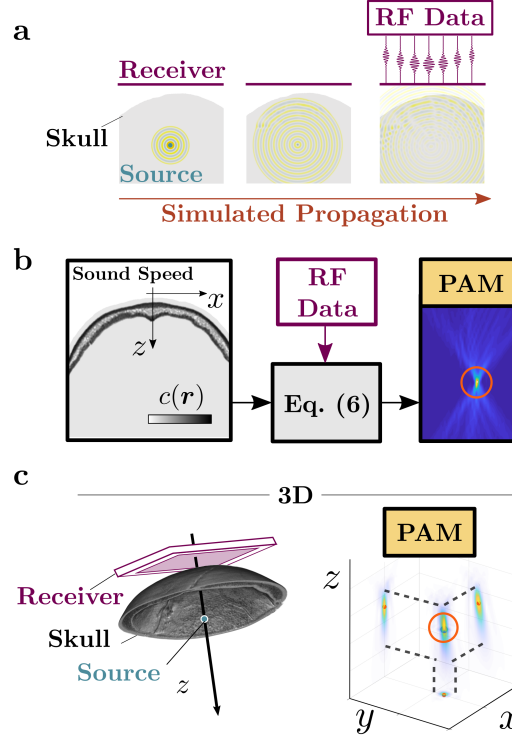


Figure 2: Flow of computations for source localization. **(a)** Trans-skull propagation from the source is simulated, and the the RF data are collected by a virtual array. **(b)** The known sound speed field $c(\mathbf{r})$ is then used with Eq. (6) to reconstruct the corrected passive acoustic maps (PAMs). The peak intensity of the PAMs (orange circle) is taken to be the source position, which is compared with the known true location from the simulation. **(c)** The reconstructions may be performed in 3D if a planar virtual array is used.

Next, the effect of focal aberration correction for the passive acoustic mapping of microbubbles was assessed. Bubbles were approximated as Gaussian sources with center frequencies of 0.4, 0.8, and 1.2 MHz (to represent harmonic components of bubbles excited with trans-skull FUS at 200 kHz or 600 kHz) [2, 5, 30]. Sources ($N = 150$) were placed randomly within a region (approximately 2 mm wide by 3 cm long) representing a vessel shape, within a sound speed environment defined from the CT data (see Fig. 5). To determine the error as a function of position and array aperture, 1 MHz sources were then individually simulated in a rectangular grid at axial positions of 30 to 80 mm, and transverse locations from -20 to 20 mm.

The resulting pressure from these sources was measured by a virtual linear array with 200 μm pitch (e.g., 250 elements for 50 mm array). The RF data $\tilde{p}(x, 0)$ were then transformed to give P_0 , from which $P(k_x, z)$ was computed with Eq. (3) or Eq. (6) as indicated, with a step size $\Delta z = 50 \mu\text{m}$. The pressure distribution was then found from $\tilde{p} = \mathcal{F}_k^{-1}[P(k_x, z)]$, and the pixel intensity field (i.e., the PAM) was computed as $I(x, z) = \|\tilde{p}(x, z)\|^2$. The convolutions in Eq. (6) were computed in the frequency domain to improve efficiency, since $P * \Lambda = \mathcal{F}_k^{-1}[\tilde{p} \cdot \lambda]$. Finally, the recovered source positions were taken to be the maxima of the generated PAMs and compared with the known source positions from the simulation. An algorithm for the reconstruction process is given in the Supplementary Material.

Because P is proportional to $\exp ik_z z$, back propagation incurs multiplication by $\exp -ik_z z$. Evanescent components of the angular spectrum, for which k_z is pure imaginary, will then grow exponentially. Therefore, all measured angular spectra P_0 were windowed with a Tukey window with cosine fraction $R = 0.25$ to taper these components [48].

Additionally, all initial spectra were zero padded such that their computational extent was four times larger than their physical extent. Sound speed fields $c(\mathbf{r})$ were padded with their edge values replicated to match the grid size of the padded P_0 . The axial step Δz was $50 \mu\text{m}$ and the field was computed from $z = 0$ to 90 mm .

4 Results

4.1 Focal Aberration Correction

First we estimated the effect of the phase correction on transmit focal accuracy for various focal targets as a function of frequency (Fig. 3). For each target focus, the focal delays were computed geometrically with Eq. (9) and then with corrections given by Eqs. (6) and (8). Across all focal positions and frequencies, the focal error was reduced from $2.1 \pm 1.2 \text{ mm}$ without phase corrections to $1.3 \pm 1.0 \text{ mm}$ with the correction. Aberration errors in focal targeting were generally larger at off-axis focal positions. See, for example the highlighted case in Fig. 3(c–e), where the uncorrected focal error was 5.1 mm , while the error for the corrected case was 0.6 mm .

We also evaluated the impact of the standoff distance of the array from the skull on focusing. Results indicate that the focal accuracy and improvement were comparable for different standoff distances ($0.6 \pm 0.3 \text{ mm}$ with the correction and $1.6 \pm 1.3 \text{ mm}$ without, see Supplementary Fig. S-1).

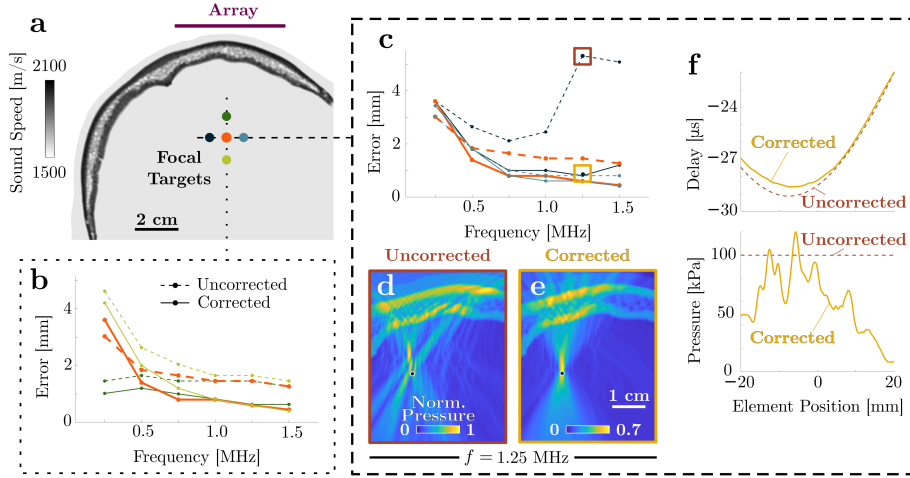


Figure 3: Use of phase corrections and amplitude shading enable improved accuracy in focal targeting. **(a)** Geometry for the simulation. Error in the position of the maximum simulated pressure compared with the target focus point with (solid lines) and without (dashed lines) the phase and amplitude corrections at different **(b)** axial and **(c)** transverse focal targets. For the outlying case at 1.25 MHz in **(c)**, the **(d)** uncorrected and **(e)** corrected maximum pressure distributions (normalized to their respective maxima) are shown, computed with **(f)** the phase corrected and uncorrected time delays and amplitude shadings.

Next we assessed the normalized (to free field) focal pressure and spot size (i.e., the total area within 3 dB of the peak pressure) achieved with the proposed aberration correction algorithm as a function frequency and position. Figure 4 illustrates how the spot size and focal pressure vary in the corrected case compared with the water path case as a function of frequency and position. The decrease in maximum pressure with frequency that is observed [Fig. 4(b–c)] reflects absorption losses that increase as f^β ($\beta = 1.2$ was used). Relative to the respective water case, the area of the focal region in the corrected trans-skull case did increase higher frequencies; however the absolute area became smaller, from $22.9 \pm 13.8 \text{ mm}^2$ for 250 kHz to $6.5 \pm 3.7 \text{ mm}^2$ for the 1.5 MHz case. Both the spot size and focal pressure were seen to vary more with the focus’ axial position than with its transverse position [compare Fig. 4(b&d) and Fig. 4(c&e)]. The focal error and spot size in the corrected and uncorrected cases averaged over all frequencies and positions are summarized in Table 1. Together, these data demonstrate that the proposed method is able to correct aberrations and improve focal targeting through the human skull.

4.2 Passive Acoustic Mapping

To assess the ability of the proposed method for PAM we estimated the errors in the peak location compared with the source position for three different frequencies (Figure 5). The total (radial) error using the heterogeneous ASA

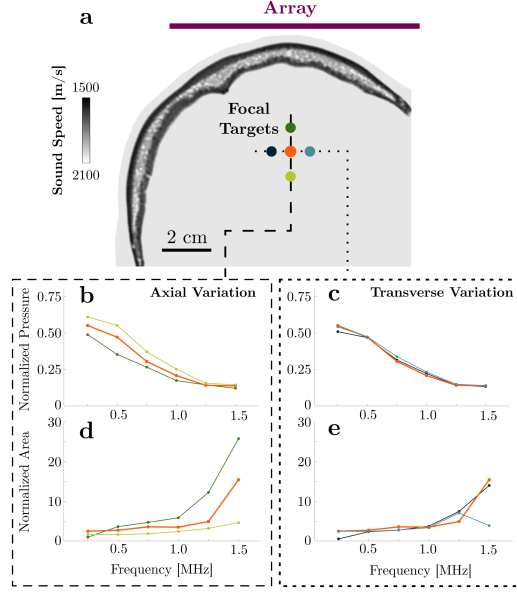


Figure 4: Corrected transmit focusing achieves focal pressures and focal spot sizes comparable to the free field case. (a) Geometry for the simulation. (b) Axial and (c) transverse variation in peak pressure amplitude as a function of frequency, normalized to amplitude obtained in simulations in water. (d) Axial and (e) transverse focal area (3 dB) normalized to the spot size obtained in the simulated water case.

Table 1: Mean and standard deviation focal location error and spot size with uncorrected [Eq. (8)] and the corrected [Eq. (9)] focusing delays, averaged over all frequencies and positions shown in Figs. 3 and 4.

Aperture	Uncorrected		Corrected	
	Error [mm]	Size [mm ²]	Error [mm]	Size [mm ²]
50 mm	2.1 ± 1.2	6.8 ± 5.7	1.3 ± 1.0	12.6 ± 16.9
100 mm	2.2 ± 0.7	7.5 ± 6.4	1.0 ± 0.4	9.6 ± 10.9

was reduced compared to that for the PAMs based on the homogeneous medium (i.e., uncorrected) ASA. Specifically, using Eq. (6), the localization errors were 1.6 ± 0.9 mm, 0.6 ± 0.4 mm, and 0.6 ± 0.5 mm for 400 kHz, 800 kHz, and 1.2 MHz sources, respectively, compared with 2.8 ± 1.5 mm, 2.0 ± 1.1 mm, and 2.2 ± 1.8 mm when Eq. (3) was used (i.e., when the presence of the skull was not accounted for). Importantly, across all simulated point sources, there were no outliers in the corrected case [e.g., in Figure 5(d), where the PAMs for the indicated sources are shown at right]. Further, the intensities of the peaks in the reconstructions were larger and more uniform in the corrected case overall: normalized to the mean corrected peak intensity for each case, the uncorrected PAMs had peak intensities of 0.94 ± 0.09 , 0.78 ± 0.12 , and 0.59 ± 0.14 for the 400 kHz, 800 kHz, and 1.2 MHz, cases respectively.

Next we assessed the localization accuracy as a function of the aperture size. For larger apertures with the same pitch (i.e., with additional elements), the localization is further improved for the corrected case. Figure 6 shows the effect of the aperture size on localization accuracy for the trans-skull case with the uncorrected ASA (top row) and corrected ASA (bottom row) for sources at 400 kHz. For the corrected case, the localization error decreases with increasing aperture size (1.5 ± 0.9 mm, 0.4 ± 0.3 mm, and 0.5 ± 0.2 mm for 50 mm, 75 mm, and 100 mm apertures, respectively). For the uncorrected case, a larger aperture does not reduce the error [2.7 ± 1.6 mm, 1.2 ± 0.8 mm, and 1.5 ± 0.6 mm for 50 mm, 75 mm, and 100 mm apertures, respectively; see Fig. 6(b–c)].

Finally, we estimated the localization error as a function of position and aperture using a rectangular grid of 1 MHz sources within the skull (Figure 7) Across all positions, the localization error was reduced by 60–80 %, and the localization error in the corrected positions decreased monotonically with aperture for the phase corrected case. Further, the peak intensity in the uncorrected case was on average 30–40 % smaller than in the corrected case. Table 2 summarizes the mean and standard deviation of the error over all points in the grid in Fig. 7. Full details, including the axial and transverse error and spot size are included in the Supplementary Tables S-1–S-3.

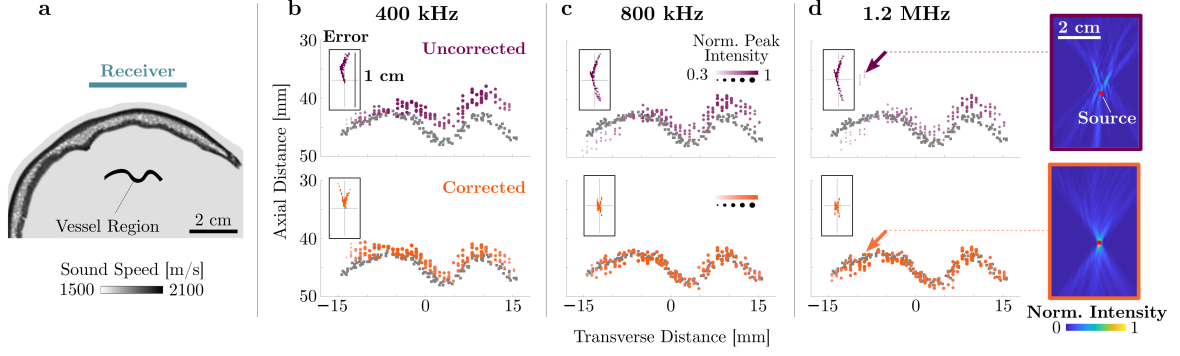


Figure 5: Accuracy of source localization for uncorrected and phase corrected trans-skull ASA PAM reconstructions. (a) Geometry of the receiver and region in which sources were randomly placed. In (b–d), gray squares represent true source positions, and circles indicate recovered location. The size and opacity of each circle indicates the intensity of the peak in the PAM, normalized to the maximum intensity for all peaks at that frequency. The insets plot each recovered source position relative to its truth position, and represent the distribution of axial and transverse errors over all reconstructions for that frequency. Peaks from PAMs computed with unmodified algorithm Eq. (3) (purple) and corrected algorithm Eq. (6) (orange) for (b) $f = 400$ kHz, (c) $f = 800$ kHz, and (d) $f = 1.2$ MHz. In (d), the normalized PAMs for the sources indicated by the arrows are shown for comparison with the true source position (red dot). Aperture for all simulations was 50 mm.

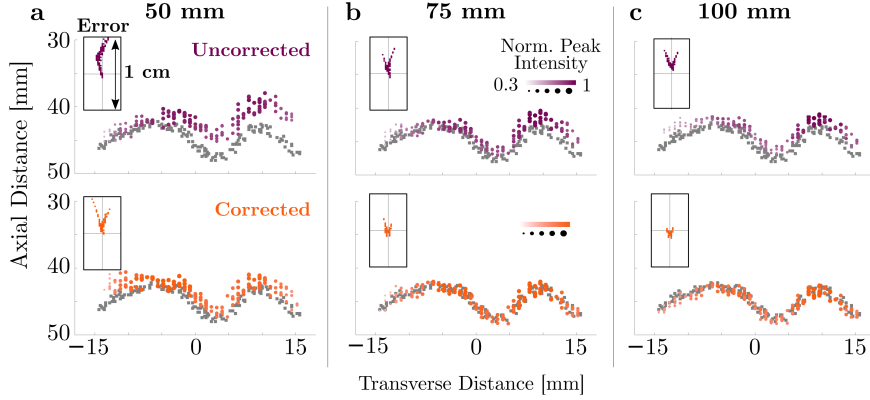


Figure 6: Phase corrected trans-skull ASA PAM reconstructions yield improved source localization accuracy and intensity compared to the uncorrected case. In (a–c), gray squares represent true source positions, and circles indicate recovered location. The size and opacity of each circle indicates the intensity of the peak in the PAM, normalized to the maximum intensity for all peaks at that frequency. The insets plot each recovered source position relative to its truth position, and represent the distribution of axial and transverse errors over all reconstructions for that frequency. Peaks from PAMs computed with unmodified algorithm Eq. (3) (purple) and corrected algorithm Eq. (6) (orange) for apertures of (a) 50 mm, (b) 75 mm, and (c) 100 mm. The frequency of all simulations sources was 400 kHz.

Table 2: Mean and standard deviation PAM localization error and peak intensities with uncorrected [Eq. (3)] and the corrected [Eq. (6)] beamforming, computed over the positions shown in Fig. 7.

Aperture	Uncorrected		Corrected	
	Error [mm]	Intensity	Error [mm]	Intensity
50 mm	3.7 ± 2.2	0.73 ± 0.46	1.2 ± 0.7	1.0 ± 0.60
75 mm	2.5 ± 1.7	0.66 ± 0.36	0.9 ± 0.5	1.0 ± 0.47
100 mm	3.5 ± 1.9	0.62 ± 0.28	0.8 ± 0.4	1.0 ± 0.39

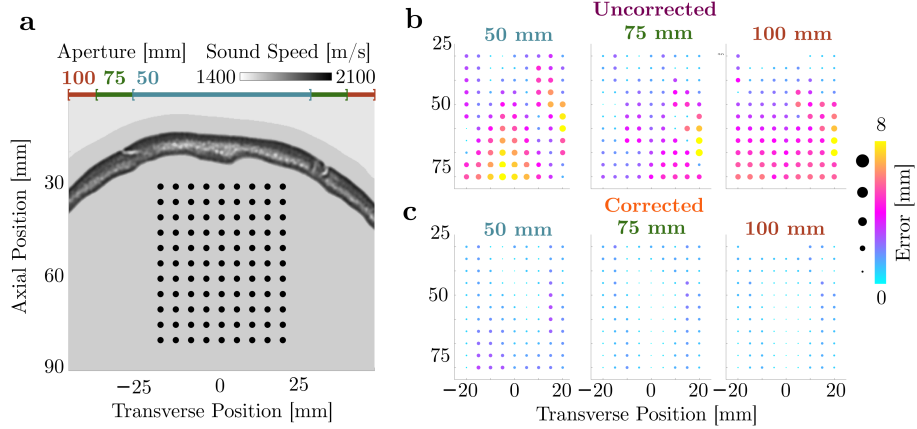


Figure 7: Source localization accuracy for phase corrected trans-skull ASA PAM reconstructions improves over 40 mm by 50 mm field of view compared to the uncorrected case for 1 MHz sources. **(a)** Sound speed field computed from CT data for a human skull, and relative position of the simulated sources (black circles) and array. Error between the location computed from the maximum value of the PAM and the true source location, for the indicated aperture size, **(b)** formed with Eq. (3) and **(c)** with Eq. (6).

4.3 Computational Efficiency

For focal aberration correction, calculation of the focusing delays and amplitudes from Eqs. (6) and (8) required 25.2 ± 8.5 ms. Note that registration of the the 2D sound speed map with the computational grid required 1.63 ± 0.03 s, but only needs to be done once during registration. For PAM, the correction using the heterogeneous ASA ([Eq. (6)]) the reconstructions took approximately 166 ± 37 ms, for a step size $\Delta z = 50 \mu\text{m}$ over all calculations. This is approximately four times slower than the uncorrected ASA [i.e., with Eq. (3)], where the computation of the PAMs required approximately 44 ± 4 ms per frequency. For a 3D PAM example case, 540 ± 18 ms was required per frequency to evaluate Eq. (6) for data from a 24-by-24 element array and $100 \mu\text{m}$ step size (173 376 voxels) and 3054 time samples. All reported times are for a standard desktop computer with no parallel processing or GPU acceleration.

5 Discussion

This work augments the ASA for sound propagation in heterogeneous media with a fast phase correction technique (Figs. 1 and 2). The methods were derived under assumptions of relatively weak heterogeneity, specifically that $|\nabla\rho_0/\rho_0 + 2\nabla c/c|$ is small compared with the wavelength (see Supplementary Material). While these conditions are not strictly met by the impedance contrast represented by the skull, our results from simulations with clinical CT data have demonstrated more than 50% reduction in localization and transmission focusing error at clinically relevant frequencies and geometries. This improvement in accuracy is on the scale of a half wavelength with little additional computational burden.

Via phase extraction and amplitude shading, the error in focal targeting was reduced by approximately 60% as compared to the uncorrected case (from 2.2 ± 0.7 mm without phase corrections to 1.0 ± 0.4 mm with the full correction—over a range of positions and frequencies, Fig. 3). The improvement in accuracy is more pronounced at higher frequencies, since the derivation assumes $c(r)$ varies slowly compared with the wavelength; thus the approximation is more valid for smaller wavelengths (higher frequencies). This is not considered as a major impediment, as aberration is more pronounced at higher frequencies, where the performance of the proposed method is favorable (Fig. 4).

Further, the method was seen to reduce the error in trans-skull source localization from computed PAMs by 60–80%, (from 2.5 ± 2.3 mm to 0.6 ± 0.5 mm) for a 1.2 MHz sources (Fig. 5). Localization accuracy was seen to increase with larger apertures (Fig. 6). A larger aperture imparts higher spatial frequency resolution (i.e., smaller Δk_x and Δk_y in the discrete transform), and thus improved coherence of the reconstruction at the correct source location. Larger apertures in the uncorrected case do not in general improve the accuracy of the localization in the presence of aberrations.

Compared with previously proposed methods for adaptation of ASA to heterogeneous media, our method has the advantage of requiring a single propagation step, and does not require transformations between each axial position [23, 27, 49]. Its inherent efficiency should allow its use in conjunction with real-time control methods based on PAM

that allow for location-specific cavitation control [40]. Moreover, the proposed algorithm is faster than full simulation methods for phase correction (e.g., 166 ms, compared with 2 minutes for the corresponding 2D k-Wave simulation). Three dimensional heterogeneous PAM examples required 520 ms per frequency for 1.7×10^5 voxels with 576 channels and 3054 time steps, which is comparable to GPU-optimized homogeneous time domain algorithms run on high performance computers (e.g., 85 ms for 10^3 voxels and 3×10^5 time samples in Ref. 38).

Computationally efficient methods may also lead to improved aberration correction accuracy by allowing iterative focal improvement. Such approaches are further supported by clinical experience that has shown that one still needs to correct for small errors (1–2 mm) during targeting. [2, 50] Currently, these corrections are calculated from CT data and confirmed via MRI-guided methods, wherein low-level focal heating (a few degrees Celsius) is measured with MR temperature imaging (MRTI) [51]. In experimental settings, aberration correction has also been confirmed by small tissue displacements (a few microns) that are induced by radiation force, using MR acoustic radiation force imaging (MR-ARFI) [52, 53]. Based on these methods, optimization routines can be developed to refine the phase of each element by maximizing focal displacement [28, 54] or focal heating for a given excitation pulse. To ensure that such adaptive focusing methods are performed in timescales similar to current CT-based methods for a single correction (of the order of seconds) the computation of the phase delays needs to take place on time scales of the order of a few milliseconds. Hence the proposed methods can also provide fast PAM for spatio-temporal control of the cerebrovascular microbubble dynamics.

Our study has some limitations. First, only a single skull has been used on our simulations; in future work we aim to evaluate the proposed approach using different skulls and skull segments. Additionally, experimental validation using different skulls, microbubbles, and phased arrays is needed for assessing the robustness of the proposed method for focal aberration correction and imaging (passive or active). Further, the algorithm is derived under the assumption of forward propagation only; extension of the method to account for reflection is nontrivial, but could improve the localization and focal targeting accuracy. The reported computation times have strong dependence on the hardware, size of the domain, and the choice of reconstruction parameters (e.g., step size, number of pad channels, etc.). However, in all cases presented it could be reduced to a few milliseconds with more sophisticated implementations, including more powerful hardware, parallel computing, and graphical processing techniques. Finally, our formulation does not include reflection, attenuation, and nonlinearity; however, the proposed method can be readily augmented to account for the effects of attenuation, [41] and nonlinearity [55, 56] potentially enabling the quantification of the acoustic emissions and the investigation of nonlinear sound propagation through heterogeneous media, albeit at the price of some additional computational burden.

6 Conclusion

We derived the general solution for the heterogeneous ASA. Numerical data showed that the general solution provides accurate trans-skull transmit focusing and point source localization. Sub-millimeter errors were attained with only a modest increase in computational complexity both for focusing and point source localization using clinically relevant frequencies (0.25–1.5 MHz) and array apertures (50–100 mm). The computation times on a standard computer were comparable to those reported for GPU-optimized uncorrected time domain algorithms on high performance computers. Collectively, our findings indicate that the heterogeneous ASA may create new possibilities for treatment, treatment monitoring, and diagnosis of brain diseases.

Appendix A Derivation of ASA Results

A.1 Governing Equation

Provided the medium is weakly heterogeneous (see Supplementary Material), propagation may be described by

$$\nabla^2 p - \frac{1}{c^2(\mathbf{r})} \frac{\partial^2 p}{\partial t^2} = 0. \quad (\text{A.1})$$

The sound speed may be written as the sum of a reference sound speed c_0 and a spatially-varying part $c'(\mathbf{r})$ [57]

$$c(\mathbf{r}) = c_0 + c'(\mathbf{r}). \quad (\text{A.2})$$

Because Eq. (A.1) is most valid for small changes in sound speed [58], the mean value of $c(\mathbf{r})$ is the natural choice for the reference sound speed c_0 . Defining $\mu(\mathbf{r}) = c_0^2/c^2(\mathbf{r})$ and taking the temporal Fourier transform of Eq. (A.1) gives

$$(\nabla^2 + k_0^2) \tilde{p} = k_0^2 (1 - \mu) \tilde{p}, \quad (\text{A.3})$$

where $k_0 = \omega/c_0$. Note that for a uniform medium, then $\mu = 1$, and Eq. (A.3) reduces to the homogeneous Helmholtz equation as expected. Now defining an auxiliary function $\lambda(\mathbf{r}) \equiv k_0^2 (1 - \mu)$, Eq. (A.3) may be written

$$(\nabla^2 + k_0^2) \tilde{p} = \mathcal{F}_k^{-1} [\Lambda * P], \quad (\text{A.4})$$

where the convolution theorem has been used, and $\Lambda(k_x, k_y, z) = \mathcal{F}_k[\lambda(x, y, z)]$. Then, since

$$\mathcal{F}_k [\nabla^2 \tilde{p}] = \left(-k_x^2 - k_y^2 + \frac{\partial^2}{\partial z^2} \right) P, \quad (\text{A.5})$$

the left hand side of Eq. (A.3) becomes

$$\begin{aligned} (\nabla^2 + k_0^2) \tilde{p} &= \nabla^2 \tilde{p} + k_0^2 \tilde{p} \\ &= \mathcal{F}_k^{-1} \left[\left(-k_x^2 - k_y^2 + \frac{\partial^2}{\partial z^2} \right) P + k_0^2 P \right] \\ &= \mathcal{F}_k^{-1} \left[\left(\underbrace{k_0^2 - k_x^2 - k_y^2}_{=k_z^2} + \frac{\partial^2}{\partial z^2} \right) P \right]. \end{aligned} \quad (\text{A.6})$$

Then Eqs. (A.4) and (A.6) yield Equation (4)

$$\begin{aligned} \mathcal{F}_k^{-1} \left[\frac{\partial^2 P}{\partial z^2} + k_z^2 P \right] &= \mathcal{F}_k^{-1} [\Lambda * P] \\ \implies \frac{\partial^2 P}{\partial z^2} + k_z^2 P &= \Lambda * P. \end{aligned} \quad (\text{A.7})$$

A.2 Implicit Solution and Approximation

Equation (A.7) may be approached in a general way by treating the right hand side as a source term and using a Green's function technique [55]. The homogeneous solution is

$$P_h = A e^{ik_z z} + B e^{-ik_z z}, \quad (\text{A.8})$$

and the appropriate Green's function for the 1D homogeneous Helmholtz equation is [59, 60]

$$g(z | z') = \frac{1}{2ik_z} \left(e^{ik_z |z-z'|} - e^{ik_z |z+z'|} \right). \quad (\text{A.9})$$

Then the full solution is then given by

$$P = P_h + \int_0^\infty g(z | z') \times \Lambda * P dz'. \quad (\text{A.10})$$

If it is assumed that there are no backward travelling waves, then $B = 0$, and from the boundary condition $P|_{z=0} = P_0$ at the source plane, the implicit solution is found [Eq. (5), repeated here]:

$$P = P_0 e^{ik_z z} + \frac{e^{ik_z z}}{2ik_z} \int_0^z e^{-ik_z z'} (\Lambda * P) dz'. \quad (\text{A.11})$$

The approximate marching scheme suggested by Jing et al. [56] defines the angular spectrum at some discrete axial position z_n to be

$$P^n = P(k_x, k_y, z_n), \quad (\text{A.12})$$

and

$$P^{n+1} = P(k_x, k_y, z_n + \Delta z). \quad (\text{A.13})$$

Then, with knowledge of the initial condition $P^0 = P_0$, the field may be approximated at arbitrary z via

$$P^{n+1} \approx P^n e^{ik_z \Delta z} + \frac{e^{ik_z \Delta z}}{2ik_z} (P^n * \Lambda) \times \Delta z. \quad (\text{A.14})$$

References

- [1] C. Demene, J. Baranger, M. Bernal, C. Delanoe, S. Auvin, V. Biran *et al.*, "Functional ultrasound imaging of brain activity in human newborns," *Science Translational Medicine*, vol. 9, no. 411, p. eaah6756, Oct. 2017.
- [2] W. J. Elias, N. Lipsman, W. G. Ondo, P. Ghanouni, Y. G. Kim, W. Lee *et al.*, "A Randomized Trial of Focused Ultrasound Thalamotomy for Essential Tremor." *The New England journal of medicine*, vol. 375, no. 8, pp. 730–739, Aug. 2016.

- [3] L. Auboire, C. A. Sennoga, J.-M. Hyvelin, F. Ossant, J.-M. Escoffre, F. Tranquart *et al.*, “Microbubbles combined with ultrasound therapy in ischemic stroke: A systematic review of in-vivo preclinical studies,” *PLOS ONE*, vol. 13, no. 2, p. e0191788, Feb. 2018.
- [4] C. D. Arvanitis, V. Askoxylakis, Y. Guo, M. Datta, J. Kloepper, G. B. Ferraro *et al.*, “Mechanisms of enhanced drug delivery in brain metastases with focused ultrasound-induced blood-tumor barrier disruption.” *Proceedings of the National Academy of Sciences of the United States of America*, vol. 115, no. 37, pp. E8717–E8726, Sep. 2018.
- [5] A. Idbaih, M. Canney, L. Belin, C. Desseaux, A. Vignot, G. Bouchoux *et al.*, “Safety and Feasibility of Repeated and Transient Blood-Brain Barrier Disruption by Pulsed Ultrasound in Patients with Recurrent Glioblastoma,” *Clinical Cancer Research*, p. clincanres.3643.2018, Jan. 2019.
- [6] C. D. Arvanitis, N. Vykhodtseva, F. Jolesz, M. Livingstone, and N. McDannold, “Cavitation-enhanced nonthermal ablation in deep brain targets: feasibility in a large animal model,” *Journal of Neurosurgery*, vol. 124, no. 5, pp. 1450–1459, May 2016.
- [7] C. D. Arvanitis, G. B. Ferraro, and R. K. Jain, “The blood–brain barrier and blood–tumour barrier in brain tumours and metastases,” *Nature Reviews Cancer*, pp. 1–16, Oct. 2019.
- [8] R. M. Jones and K. Hynynen, “Advances in acoustic monitoring and control of focused ultrasound-mediated increases in blood-brain barrier permeability,” *The British Journal of Radiology*, vol. 92, no. 1096, p. 20180601, Apr. 2019.
- [9] C. Demene, J. Robin, M. Pernot, F. Perren, and M. Tanter, “Transcranial ultrasound localization microscopy reveals sub-resolution blood dynamics in aneurysms and stenosis in the adult human brain,” in *IEEE International Ultrasonics Symposium*, Glasgow, Scotland, UK, Oct. 6-9 2019.
- [10] C. Errico, J. Pierre, S. Pezet, Y. Desailly, Z. Lenkei, O. Couture *et al.*, “Ultrafast ultrasound localization microscopy for deep super-resolution vascular imaging,” *Nature*, vol. 527, no. 7579, pp. 499–502, Nov. 2015.
- [11] M. A. O’Reilly and K. Hynynen, “A super-resolution ultrasound method for brain vascular mapping,” *Medical Physics*, vol. 40, no. 11, p. 110701, 2013.
- [12] M. Pernot, G. Montaldo, M. Tanter, and M. Fink, ““Ultrasonic stars” for time-reversal focusing using induced cavitation bubbles,” *Applied Physics Letters*, vol. 88, no. 3, p. 034102, Jan. 2006.
- [13] K. J. Haworth, J. B. Fowlkes, P. L. Carson, and O. D. Kripfgans, “Towards Aberration Correction of Transcranial Ultrasound Using Acoustic Droplet Vaporization,” *Ultrasound in Medicine & Biology*, vol. 34, no. 3, pp. 435–445, Mar. 2008.
- [14] J. Gâteau, L. Marsac, M. Pernot, J. Aubry, M. Tanter, and M. Fink, “Transcranial Ultrasonic Therapy Based on Time Reversal of Acoustically Induced Cavitation Bubble Signature,” *IEEE Transactions on Biomedical Engineering*, vol. 57, no. 1, pp. 134–144, Jan. 2010.
- [15] A. Kyriakou, E. Neufeld, B. Werner, M. M. Paulides, G. Szekely, and N. Kuster, “A review of numerical and experimental compensation techniques for skull-induced phase aberrations in transcranial focused ultrasound,” *International Journal of Hyperthermia*, vol. 30, no. 1, pp. 36–46, Feb. 2014.
- [16] M. A. O’Reilly, R. M. Jones, and K. Hynynen, “Investigating a method for non-invasive ultrasound aberration correction through the skull bone,” in *Medical Imaging 2014: Ultrasonic Imaging and Tomography*, vol. 9040. International Society for Optics and Photonics, Mar. 2014, p. 904013.
- [17] J. Thomas and M. A. Fink, “Ultrasonic beam focusing through tissue inhomogeneities with a time reversal mirror: application to transskull therapy,” *IEEE Transactions on Ultrasonics, Ferroelectrics, and Frequency Control*, vol. 43, no. 6, pp. 1122–1129, Nov. 1996.
- [18] K. Hynynen and F. A. Jolesz, “Demonstration of Potential Noninvasive Ultrasound Brain Therapy Through an Intact Skull,” *Ultrasound in Medicine & Biology*, vol. 24, no. 2, pp. 275–283, Feb. 1998.
- [19] J. White, G. T. Clement, and K. Hynynen, “Transcranial ultrasound focus reconstruction with phase and amplitude correction,” *IEEE Transactions on Ultrasonics, Ferroelectrics, and Frequency Control*, vol. 52, no. 9, pp. 1518–1522, Sep. 2005.

- [20] M. Pernot, J.-F. Aubry, M. Tanter, A.-L. Boch, F. Marquet, M. Kujas *et al.*, “In vivo transcranial brain surgery with an ultrasonic time reversal mirror,” *Journal of Neurosurgery*, vol. 106, no. 6, pp. 1061–1066, Jun. 2007.
- [21] J.-F. Aubry, M. Tanter, M. Pernot, J.-L. Thomas, and M. Fink, “Experimental demonstration of noninvasive transskull adaptive focusing based on prior computed tomography scans,” *The Journal of the Acoustical Society of America*, vol. 113, no. 1, pp. 84–93, Jan. 2003.
- [22] A. Pulkkinen, B. Werner, E. Martin, and K. Hynynen, “Numerical simulations of clinical focused ultrasound functional neurosurgery,” *Physics in Medicine and Biology*, vol. 59, no. 7, pp. 1679–1700, Mar. 2014.
- [23] G. T. Clement and K. Hynynen, “A non-invasive method for focusing ultrasound through the human skull,” *Physics in Medicine and Biology*, vol. 47, no. 8, pp. 1219–1236, Apr. 2002.
- [24] M. Tabei, T. D. Mast, and R. C. Waag, “Simulation of ultrasonic focus aberration and correction through human tissue,” *The Journal of the Acoustical Society of America*, vol. 113, no. 2, pp. 1166–1176, Jan. 2003.
- [25] N. McDannold, G. T. Clement, P. Black, F. Jolesz, and K. Hynynen, “Transcranial Magnetic Resonance Imaging–Guided Focused Ultrasound Surgery of Brain Tumors: Initial Findings in 3 Patients,” *Neurosurgery*, vol. 66, no. 2, pp. 323–332, Feb. 2010.
- [26] R. M. Jones and K. Hynynen, “Comparison of analytical and numerical approaches for CT-based aberration correction in transcranial passive acoustic imaging,” *Physics in Medicine and Biology*, vol. 61, no. 1, pp. 23–36, Nov. 2015.
- [27] U. Vyas and D. Christensen, “Ultrasound beam simulations in inhomogeneous tissue geometries using the hybrid angular spectrum method,” *IEEE Transactions on Ultrasonics, Ferroelectrics, and Frequency Control*, vol. 59, no. 6, pp. 1093–1100, Jun. 2012.
- [28] U. Vyas, E. Kaye, and K. B. Pauly, “Transcranial phase aberration correction using beam simulations and MR-ARFI,” *Medical Physics*, vol. 41, no. 3, p. 032901, Mar. 2014.
- [29] S. A. Leung, T. D. Webb, R. R. Bitton, P. Ghanouni, and K. B. Pauly, “A rapid beam simulation framework for transcranial focused ultrasound,” *Scientific Reports*, vol. 9, no. 1, pp. 1–11, May 2019.
- [30] C. D. Arvanitis, C. Crake, N. McDannold, and G. T. Clement, “Passive Acoustic Mapping with the Angular Spectrum Method,” *IEEE Transactions on Medical Imaging*, vol. 36, no. 4, pp. 983–993, Apr. 2017.
- [31] M. Gyöngy and C. C. Coussios, “Passive Spatial Mapping of Inertial Cavitation During HIFU Exposure,” *IEEE Transactions on Biomedical Engineering*, vol. 57, no. 1, pp. 48–56, Jan. 2010.
- [32] C. Coviello, R. Kozick, J. Choi, M. Gyöngy, C. Jensen, P. P. Smith *et al.*, “Passive acoustic mapping utilizing optimal beamforming in ultrasound therapy monitoring,” *The Journal of the Acoustical Society of America*, vol. 137, no. 5, pp. 2573–2585, May 2015.
- [33] K. J. Haworth, K. B. Bader, K. T. Rich, C. K. Holland, and T. D. Mast, “Quantitative Frequency-Domain Passive Cavitation Imaging,” *IEEE Transactions on Ultrasonics, Ferroelectrics, and Frequency Control*, vol. 64, no. 1, pp. 177–191, Jan. 2017.
- [34] R. M. Jones, M. A. O’Reilly, and K. Hynynen, “Transcranial passive acoustic mapping with hemispherical sparse arrays using CT-based skull-specific aberration corrections: a simulation study,” *Physics in Medicine & Biology*, vol. 58, no. 14, p. 4981, 2013.
- [35] M. A. O’Reilly, R. M. Jones, and K. Hynynen, “Three-Dimensional Transcranial Ultrasound Imaging of Microbubble Clouds Using a Sparse Hemispherical Array,” *IEEE Transactions on Biomedical Engineering*, vol. 61, no. 4, pp. 1285–1294, Apr. 2014.
- [36] L. Deng, M. A. O’Reilly, R. M. Jones, R. An, and K. Hynynen, “A multi-frequency sparse hemispherical ultrasound phased array for microbubble-mediated transcranial therapy and simultaneous cavitation mapping,” *Physics in Medicine & Biology*, vol. 61, no. 24, p. 8476, 2016.
- [37] C. D. Arvanitis, G. T. Clement, and N. McDannold, “Transcranial Assessment and Visualization of Acoustic Cavitation: Modeling and Experimental Validation,” *IEEE Transactions on Medical Imaging*, vol. 34, no. 6, pp. 1270–1281, Jun. 2015.

- [38] R. M. Jones, L. Deng, K. Leung, D. McMahon, M. A. O'Reilly, and K. Hynynen, "Three-dimensional transcranial microbubble imaging for guiding volumetric ultrasound-mediated blood-brain barrier opening," *Theranostics*, vol. 8, no. 11, pp. 2909–2926, 2018.
- [39] R. M. Jones, M. A. O'Reilly, and K. Hynynen, "Experimental demonstration of passive acoustic imaging in the human skull cavity using CT-based aberration corrections," *Medical Physics*, vol. 42, no. 7, pp. 4385–4400, Jul. 2015.
- [40] A. Patel, S. J. S. Jr, and C. D. Arvanitis, "Closed Loop Spatial and Temporal Control of Cavitation Activity with Passive Acoustic Mapping," *IEEE Transactions on Biomedical Engineering*, pp. 1–1, 2018.
- [41] J. Gu and Y. Jing, "Numerical Modeling of Ultrasound Propagation in Weakly Heterogeneous Media Using a Mixed-Domain Method," *IEEE Transactions on Ultrasonics, Ferroelectrics, and Frequency Control*, vol. 65, no. 7, pp. 1258–1267, Jul. 2018.
- [42] B. E. Treeby and B. T. Cox, "k-Wave: MATLAB toolbox for the simulation and reconstruction of photoacoustic wave fields," *Journal of Biomedical Optics*, vol. 15, no. 2, p. 021314, Apr. 2010.
- [43] G. T. Clement, P. J. White, and K. Hynynen, "Enhanced ultrasound transmission through the human skull using shear mode conversion," *The Journal of the Acoustical Society of America*, vol. 115, no. 3, pp. 1356–1364, Feb. 2004.
- [44] B. E. Treeby and B. T. Cox, "Modeling power law absorption and dispersion for acoustic propagation using the fractional Laplacian," *The Journal of the Acoustical Society of America*, vol. 127, no. 5, pp. 2741–2748, May 2010.
- [45] R. S. C. Cobbold, *Foundations of Biomedical Ultrasound*. Oxford University Press, 2007.
- [46] F. Marquet, A.-L. Boch, M. Pernot, G. Montaldo, D. Seilhean, M. Fink *et al.*, "Non-invasive ultrasonic surgery of the brain in non-human primates," *The Journal of the Acoustical Society of America*, vol. 134, no. 2, pp. 1632–1639, Aug. 2013.
- [47] S.-Y. Wu, C. Aurup, C. S. Sanchez, J. Grondin, W. Zheng, H. Kamimura *et al.*, "Efficient Blood-Brain Barrier Opening in Primates with Neuronavigation-Guided Ultrasound and Real-Time Acoustic Mapping," *Scientific Reports*, vol. 8, no. 1, p. 7978, May 2018.
- [48] E. Williams, *Fourier Acoustics*. Elsevier, 1999.
- [49] G. T. Clement and K. Hynynen, "Forward planar projection through layered media," *IEEE Transactions on Ultrasonics, Ferroelectrics, and Frequency Control*, vol. 50, no. 12, pp. 1689–1698, Dec. 2003.
- [50] W. J. Elias, D. Huss, T. Voss, J. Loomba, M. Khaled, E. Zadicario *et al.*, "A pilot study of focused ultrasound thalamotomy for essential tremor," *The New England Journal of Medicine*, vol. 369, no. 7, pp. 640–648, Aug. 2013.
- [51] E. Martin, D. Jeanmonod, A. Morel, E. Zadicario, and B. Werner, "High-intensity focused ultrasound for noninvasive functional neurosurgery," *Annals of Neurology*, vol. 66, no. 6, pp. 858–861, 2009.
- [52] E. A. Kaye and K. B. Pauly, "Adapting MRI acoustic radiation force imaging for in vivo human brain focused ultrasound applications," *Magnetic Resonance in Medicine*, vol. 69, no. 3, pp. 724–733, 2013.
- [53] N. McDannold and S. E. Maier, "Magnetic resonance acoustic radiation force imaging," *Medical Physics*, vol. 35, no. 8, pp. 3748–3758, Aug. 2008.
- [54] L. Marsac, D. Chauvet, B. Larrat, M. Pernot, B. Robert, M. Fink *et al.*, "MR-guided adaptive focusing of therapeutic ultrasound beams in the human head," *Medical Physics*, vol. 39, no. 2, pp. 1141–1149, 2012.
- [55] Y. Jing, M. Tao, and G. T. Clement, "Evaluation of a wave-vector-frequency-domain method for nonlinear wave propagation," *The Journal of the Acoustical Society of America*, vol. 129, no. 1, pp. 32–46, Jan. 2011.
- [56] Y. Jing, M. Tao, and J. Cannata, "An improved wave-vector frequency-domain method for nonlinear wave modeling," *IEEE Transactions on Ultrasonics, Ferroelectrics, and Frequency Control*, vol. 61, no. 3, pp. 515–524, Mar. 2014.
- [57] G. P. Agrawal and C. L. Mehta, "Angular Spectrum Approach to Electromagnetic Wave propagation in Inhomogeneous Media," *Optics Communications*, vol. 14, no. 1, pp. 88–91, May 1975.

- [58] P. G. Bergmann, "The Wave Equation in a Medium with a Variable Index of Refraction," *The Journal of the Acoustical Society of America*, vol. 17, no. 4, pp. 329–333, Apr. 1946.
- [59] K. Watanabe, *Integral Transform Techniques for Green's Function*, 2nd ed., ser. Lecture Notes in Applied and Computational Mechanics. Springer International Publishing, 2015.
- [60] P. M. Morse, H. Feshbach, and G. P. Harnwell, *Methods of Theoretical Physics, Part I*. Boston, Mass: McGraw-Hill Book Company, Jun. 1953.